Microchannel scaffolds for neural signal acquisition and analysis

Rouhollah Habibey, Asiyeh Golabchi and Axel Blau [§]

Fondazione Istituto Italiano di Tecnologia (IIT), Dept. of Neuroscience and Brain Technologies (NBT), Neurotechnologies (NTech), Via Morego 30, 16163 Genoa, Italy, www.iit.it
[§]Corresponding author's email address: axel.blau@iit.it

Abstract. Replica-casting finds wide application in soft lithography [17] and microfluidics [4]. Most commonly, structures are molded with micro- to nano-patterned photoresists as master casts into polydimethylsiloxane (PDMS). PDMS features many favorable properties. It reproduces geometric details with nanometer fidelity, has low cytotoxicity and is transparent in the visible spectrum. It is furthermore biostable both *in vitro* and *in vivo*, can be plasma-bonded to itself, has low water permeability and is easy to handle and process. After curing, the PDMS can be peeled from the master and latter usually be reused [1] if patterns are not undercut [24]. Here, we describe the straightforward replica-molding process for devices that can be exploited either as perforated microchannel scaffolds for the *in vitro* use in axonal guidance and regeneration studies on microelectrode arrays (MEAs) or for the production of tissue-conformal *in vivo* MEAs for neuroprosthetic applications.

1 Introduction

In microfluidics, PDMS microchannel systems inspired by Taylor *et al.*, allow the separation of somata from their axons in two different fluidic environments [20]. Over the last decade, devices like these have been extensively utilized for studying axonal injury and regeneration, myelination, protein and mRNA synthesis, as well as transport phenomena [3, 10, 11, 16, 23]. Inexpensive microlithography techniques for the generation of microtunnels have been used recently to structure networks in variable spatial designs. They allow microwell-confined populations of neural networks to connect through microchannels [22]. Microchannels can also be utilized in electrophysiological studies of neural networks *in vitro* by placing cells in specific substrate locations including the electrodes [7, 18]. By combining microchannels with microelectrode arrays (MEAs), activity can be selectively recorded from axons. In addition, amplitudes of extracellularly recorded signals from neurites are usually amplified by two orders of magnitude (millivolts instead of tens of microvolts) [21] [8]. In a non-conventional fabrication scheme, microchannel devices can also be transformed into MEAs. Filling the cavities of multi-level microchannel scaffolds with electrically conductive polymers or composite materials is a rapid prototyping approach for the design of various *in vitro* and *in vivo* recording and stimulation devices [5]. This

opens the door for both application-specific prototyping as well as mass production of more tissue-mimetic neuroprosthetic recording and stimulation devices. After a brief methodological description of the general device fabrication steps, we present exemplary results on device exploitation as physical cell culture guidance cues and as MEAs for neuroprosthetics.

2 Methods

2.1 Fabrication of multi-level PDMS microchannel devices

Bi-level patterns can be casted into high-aspect ratio negative photoresist (*e.g.*, SU-8) in a two-step photolithography technique using separate masks (Expert, Silvaco). To generate both microchannels and perforating vias, the first mask defines all features, whereas the second mask delineates the through-holes only. The principle fabrication steps and overall process flow are depicted in **Fig. 1**: A clean silicon wafer (A) is spin-coated with the first photo resin layer (<150 µm) (B) and photo cross-linked through a first photomask to define both the channels and the sockets for vias (C). The procedure is repeated in (D) and (E) for the second photoresist layer (< 150 µm) to define the via through-holes. After removing the uncured photoresin in a developing step (F), the bi-level microstructure (G) can be covered with PDMS pre-polymer (H), cured after its leveling, and be peeled off to result in a microchannel scaffold with via holes (I). Such microchannels can either be used as physical guidance cues for axons and dendrites or be filled with conductive polymers (*e.g.*, PEDOT:PSS, carbon-polymer composites) (J) and backside-insulated (K) to yield all-polymer MEAs (*polyMEA*s) with electrodes and contact pads at the via holes for their application *in vitro* or *in vivo* (L).

2.2 Conductive materials

If not stated differently, all materials were purchased from Sigma-Aldrich. A composite of carbon, graphite, and poly (3,4- ethylenedioxythiophene):polystyrene sodium sulfonate (PEDOT:PSS) (p Jet 700, Clevios) with up to 5% of conductivity enhancers was used as a rubber-like electrode-, conductive track- and connection pad-filling. The carbon/graphite/PEDOT:PSS composite was mixed into pre-mixed PDMS pre-polymer and curing agent (Sylgard 184, Dow Corning) in a 1:1:3 ratio until its DC resistivity dropped below 10 kΩ over a distance of 5 mm. The track-, contact pad- and electrode-cavities were filled with the conductive material by spreading it onto the *polyMEA* scaffold. Excess material was removed by first swiping the surface with the edge of a ruler, then with a cotton swab and filter paper. This procedure removed the shortcuts between pads and tracks. In a final step, the surface of the *polyMEA* was cleaned by rolling a lint remover over it. To ensure that no shortcuts had remained, adjacent contact pads were probed by an ohmmeter. The conductive composite was cured at 120 °C for one hour. The *polyMEA*s were then backside-insulated by a second layer of PDMS. The contact pads of *in vivo polyMEA* probes were slid between the pins of Omnetics connectors. A folded laser transparency between the folded

polyMEA helped in pressing the pads against the connector pins, thereby establishing electrical contact. A thin PDMS coat can be used for pad/pin insulation thereafter. Device biocompatibility was tested in cell culture. The electrical characteristics were determined by electrical impedance spectroscopy. *PolyMEA* recording functionality was validated with cortical cultures after 7 days *in vitro* (DIV).

2.3 Electrochemical characterization of *polyMEA* electrodes

The electrodes of *polyMEA*s were characterized by electrochemical impedance spectroscopy (EIS). The *polyMEA*s were placed in a custom-made Faraday box and their pads sequentially connected by a gold-coated spring-contact probe. The electrodes were immersed in saturated KCl at room temperature. A silver/silver chloride wire (Ø1 mm) was used as a reference electrode and a Pt sheet ($\sim 2 \times 3\ mm^2$) as the counter electrode. Impedance spectroscopy was performed at frequencies between 1 Hz and 100 kHz (Perstat 2273, Princeton Applied Research).

2.4 Cell culture

If not stated differently, all cell culture chemicals were purchased from Invitrogen. PDMS *in vitro polyMEA*s and commercial MEAs (Multi Channel Systems), PDMS caps [6] and PDMS microchannel tiles were autoclaved at 120 °Ċ for 20 minutes before being moved to the sterile hood. To increase their surface hydrophilicity, MEAs and *polyMEA*s were exposed to oxygen plasma (0.5-2 min, 50 W, 2.45 GHz, 0.3 mbar O_2) [femto, Diener]. Their central surface was then coated with 20 µl of 0.1 mg/ml poly-D-lysine (PDL) and 0.05 mg/ml laminin, which was allowed to dry in vacuum. To remove soluble PDL, MEAs were rinsed twice with sterile ultrapure water and dried. After complete water evaporation, the PDMS microchannels were aligned on the surface of the commercial MEAs using a sterile water droplet. The crossing points of the microchannels were placed on the electrodes. Therefore, every microchannel included eight electrodes in one row or column (*e.g.*, 68 to 61 in **Fig. 2**). Cell suspensions (rat E18) were prepared following standard protocols [3]. For microchannel devices on commercial MEAs, a small drop (~5 µL; 10,600 cortical neurons/µL, ~ 50,000 cells per device) was placed into just one out of four reservoirs. On *polyMEA*s, about 100,000 cells were plated onto their central electrode area. Cells were allowed to settle for 30 min in a cell culture incubator (5% CO_2, 37 °C, 95% RH) before adding 1 ml of serum-free medium (Neurobasal medium, B27 2%, Glutamax 1%, penicillin/streptomycin 1%). Cultures were protected by a PDMS cap against evaporation and contamination [6] and stored in the incubator. Every week, 450 µL of media was exchanged with fresh warm media. Cultures were imaged once a week on an inverted microscope (DMIL, Leica Microsystems) equipped with a 5 megapixel camera (DFC420C, Leica Microsystems).

2.5 Electrophysiology

Extracellular signals were recorded with a 60-channel filter-amplifier (MEA60-Up, Multi Channel Systems), featuring a built-in thermal sensor and heating element. For microchannel tiles, acquired activity (MC_Rack, Multi Channel Systems) was filtered and analyzed offline. The low frequency noise, which was augmented by the microchannels, was removed by a second-order Bessel high-pass filter (cut-off at 200 Hz). Spikes were detected in the filtered data stream by passing a negative threshold set to ±4.5 StDev of the peak-to-peak noise. Only downward threshold-crossings were analyzed.

2.6 Statistical analysis

Spike trains from microchannel tile recordings were transformed to timestamps (NeuroExplorer, Nex Technologies) for mean frequency and burst analysis. Individual units on each electrode were detected by k-means clustering (Offline Sorter, Plexon). Thereafter, sorted units were checked visually to merge the same units or exclude unsorted rare signals from analysis. Numerical results were further analyzed by a one-way repeated measures analysis of variance (ANOVA) or a two-way ANOVA, followed by a Bonferroni post-test for all groups (Prism, GraphPad). A probability of $p < 0.05$ was considered significant. Data are expressed as mean ± SEM or as quartiles (Whisker-bars) with maximum and minimum values.

3 Results

3.1 Recording activity from microchannel-confined axons

Cells started to grow their neurites into the microchannels after 3 DIV. After 9 DIV, axons had almost passed through the entire channel and entered into one of the three axonal compartments (**Fig. 2**). The neuronal tissue mass inside the channels was increasing up to 27 DIV. Afterward, neural tissue inside the channels and the axonal compartments started to degenerate and thick axonal bundles appeared (**Fig. 8**C).
Because the microchannels were aligned with the electrodes, axons were forced to grow over the electrodes. The small microchannel cross sections (40 µm x 5 µm) increased the electrical resistance to ground, thereby amplifying the weak extracellular axonal signals. At 9 DIV, first signals could be recorded. They were similar in shape to random networks, but had higher amplitudes (>100 µV; **Fig. 3**A). The signal amplitudes increased up to 600 µV after 20 DIV (**Fig. 3**B). The microchannels not only allowed to record from axons, but also forced the same axon to pass over or nearby all electrodes in one row of the electrode array (**Fig. 2**C; *e.g.*, electrodes 28 to 21). This made it possible to record from the same axon at its different lengths. Therefore, the same signal appeared with short delay on subsequent electrodes as it propagated along the axon (**Fig. 3**).

Compared to the diameter of an axon (~1 µm), the width of a microchannel was sufficiently large (40 µm) to let different axonal branches from the same network enter into it. Therefore, every electrode inside the microchannel could simultaneously record from different axons. Signals were sorted by shape to distinguish between the different axons (sources) (**Fig. 4**A-C). In general, two main signal categories were detected inside the microchannels; monophasic signals (mainly with negative wave) and biphasic signals (mainly with a negative followed by a positive wave). In contrast to quickly decaying biphasic signals, monophasic signals could propagate to distant electrodes inside a microchannel. This feature was amplitude-independent (**Fig. 4**B). Overlaying the signals recorded from subsequent electrodes inside the same channel showed the propagation delay and how the signal shape varied with location (**Fig. 4**C).

To analyze the network activity evolution and the propagation velocity along the axons inside the microchannels over time, the electrical activity at 10, 20, 30 and 53 DIV was compared. To evaluate how activity levels change over time or along channels, two subsequent electrodes in a channel were considered as one segment, thereby dividing every channel into the following four segments: Seg 1(0-250 µm), Seg 2 (250-650 µm), Seg 3 (650-1050 µm) and Seg 4 (1050-1300 µm) (Fig. **5** a). Because the amplifiers for electrodes 27, 52 and 62 were switched off at 10 and 20 DIV, data for the respective segments was collected on these two days from one electrode only. A comparison of the overall number of spikes per minute in the proximal segments of all considered channels with that of their distal segments showed that the signal frequency decreases along the channel for all recording days ($p < 0.001$ at 10 and 30 DIV, $p < 0.01$ at 20 DIV; Fig. **5**B). Monitoring the mean signal frequency in each segment over time (Fig 4C) showed a significant decrease at 53 DIV compared to 10 DIV in segments 1, 2 and 3 ($p < 0.05$).

Signal frequencies and propagation velocities were evaluated in detail for three selected channels (channel 2 (electrodes 21-28), 5 (electrodes 51-58) and 6 (electrodes 61-68)). The mean signal frequency for each channel was calculated by averaging all recorded signals from any of the electrodes inside a single channel. The mean signal frequency for each channel tended to decrease over time. This decrease was significant between 10 DIV and the subsequent DIVs for channel 5 ($p < 0.05$ vs. 20 and 30 DIV, and $p < 0.001$ vs. 53 DIV; **Fig. 6**A) and channel 6 ($p < 0.05$ vs. 30 DIV and $p < 0.01$ vs. 53 DIV; Fig 5A). The propagation velocity was calculated by dividing the constant distance between a pair of electrodes (200 µm) by the temporal delay of the signal appearance on two subsequent electrodes. The mean propagation velocity for each channel was calculated by averaging the propagation velocities of all subsequent electrode pairs in a channel. For electrodes from which no signals were acquired an 10 and 20 DIV (electrodes 27, 52 and 62), the average velocity was calculated for the two nearest electrodes (channel 2; electrodes 28 and 26, and channel 6; electrodes 63 and 61). The mean propagation velocity tended to increase with culture age, which was contrary to the observed decrease in the spike frequency (**Fig. 6**A and B). Propagation velocity clearly increased with respect to 10 DIV in channel 2 ($p < 0.001$ vs. 20 DIV and $p < 0.01$ vs. 53 DIV; **Fig. 6**B), channel 5 ($p < 0.05$,

$p < 0.001$ and $p < 0.001$ vs. 20, 30 and 53 DIV, respectively; **Fig. 6**B) and channel 6 ($p < 0.001$ vs. 20, 30 and 53 DIV; **Fig. 6**B). This increase was also significant when compared between 20 DIV and the subsequent recording days at 30 and 53 DIV in all channels ($p < 0.001$; **Fig. 6**B).

In addition to determining the mean propagation velocity, the changes in the propagation velocity along the axon was calculated by comparing the velocity propagation between subsequent electrode pairs (**Fig. 7**). In channel 5, only few signals propagated along the entire length of the channel at 10, 20 and 53 DIV. Therefore, these DIVs were excluded from the analysis. Despite variations in the propagation velocities along channels 2 and 5, they were not significant between two adjacent segments on any of the recording DIVs (**Fig. 7**A and B). However, in channel 6, significant changes in the propagation velocity were observed between different segments, which could either decrease (*e.g.*, $p < 0.001$ from 68-67 to 67-66 at 30 DIV; **Fig. 7**C) or increase (*e.g.*, $p < 0.001$ from 68-67 to 67-66 at 53 DIV; **Fig. 7**C). Besides the local fluctuations in velocity, an increase in velocity over time is clearly evident for all channels in **Fig. 7**.

Bursts propagation was analyzed for channels 2, 5 and 6 using the following criteria in NeuroExplorer: maximal interval to start burst = 0.02 s, maximal interval to end burst = 0.01 s, minimal interval between bursts = 0.01 s, minimal duration of burst = 0.02 s, minimal number of spikes in burst = 4, and bin size = 1 s). **Fig. 8** summarizes the mean burst rate in different segments of channels 2, 5 and 6. At 10 DIV, only a few bursts were detected (**Fig. 8**B). The burst frequency (bursts/min) increased over time and reached its maximum value after 30 DIV (**Fig. 8**B). A burst rate analysis for each segment of these three channels showed that bursts faded after 400-600 µm propagation length within a channel (**Fig. 8**B). The burst rate in segments 3 and 4 was significantly lower than in segment 1 ($p < 0.01$ and $p < 0.05$ at 20 DIV, $p < 0.001$ at 30 DIV, and $p < 0.001$ at 53 DIV; **Fig. 8**B).

3.2 *polyMEA* features and device characteristics

Most deep brain implants are designed to record from biological tissue at near cellular resolution. This requires the electrode diameters to be on a similar scale. The design considerations for the implantable polymer microelectrode arrays included: 1) compatibility to commercial or custom-made signal processing electronics; 2) preferably a seamless, flexible and stable connection between implanted electrodes and the electronic platform; 3) an insertion depth control that may be defined by the probe geometry and guidance features (e.g., shaft edges, stoppers, ...).

Once geometries and boundary conditions are defined, photomasks can be designed by any microelectromechanical systems (MEMS) layout editor (*e.g.*, Expert, Silvaco; CleWin, WieWeb). Exemplarily, five different *polyMEA* designs for different brain areas are depicted in **Fig. 9**. Overall device features and the connecting scheme for a low-density electrode *polyMEA* are shown in **Fig. 10**. Its feature sizes are summarized in **Table 1**.

3.3 Electrical characteristics of carbon-, graphite-, PEDOT:PSS-in-PDMS composite electrodes

In the *in vivo polyMEA* featuring a 2 x 9 electrode array, all 18 microelectrodes were functional. The average and extreme electrode impedance distribution between 1 Hz and 100 kHz, is depicted in **Fig. 11**. Impedances ranged between 5 MΩ at low frequencies and several hundred kΩ at 1 kHz. Electrodes had almost resistive character at 1 kHz.

4 Discussion

The presented examples demonstrated how a straightforward replica-molding process for PDMS sheets generates perforated microchannel scaffolds for diverse applications. We exemplarily discussed their *in vitro* use in axonal guidance and regeneration studies on microelectrode arrays (MEAs) and the production of tissue-conformal *in vivo* MEAs for neuroprosthetic applications.

4.1 PDMS microchannels for axon guidance and electrophysiology

We showed that axons can be easily guided in microchannels that were aligned on top of the recording electrodes of a MEA. This allowed the detailed evaluation of axonal morphology, the different types of activity and their propagation velocity along channels over time.

We found that the signal frequency decreased between proximal and distal segments of a microchannel. This could have two reasons: the signal could be fading along the channel as it was evident in most cases (**Fig. 3**B). Furthermore, axons may leave the straight path by changing their growth direction at the channel crossing points (**Fig. 2**B).

The effect of microchannel geometry on signal quality has been evaluated by Wang *et al*. [21]. They showed that in microchannels with lengths between 200 µm and 3000 µm the signal amplitude decreases along the channel length. Therefore, signals could become too small to be detected by electrodes in distal sections. In accordance with **Fig. 3**, large amplitude signals in proximal sections (electrode 68) decreased as they propagated within the channel. In line with the findings by Wang *et al.* [21], the high microchannel resistance combined with its stray capacitance acted like a first-order low-pass filter that attenuate high frequency signal amplitudes (i.e. the negative peaks of an action potential). Equally, the channel cross-section can affect signal properties [21]. Although all microchannels had the same cross-section, the number of axons and the thickness of the axon bundles inside the microchannel varied with channel depth and over time, thereby changing the total cross-section of a microchannel at different channel locations. In 2009, Dworak and Wheeler showed that the growth of neurites inside microchannels (750x10x3 μm^3) increased the resistivity from 75 Ω cm of empty channels to 300 Ω cm for microchannels filled with neural tissue due to an effective decrease of the channel cross-section [8].

The increase of neural tissue mass inside the microchannels between 20 and 30 DIVs (**Fig. 8**C) could be correlated with an increased spike frequency for almost all channels and all channel segments (Fig. **5** and **Fig. 6**). Equally, a decrease in neural tissue density after 53 DIV led to a decrease in the firing frequency in all channels (Fig. **5** and **Fig. 6**). A significant decrease of the signal frequency after 30 DIV in all segments could be related to the axonal degeneration and the formation of axonal bundles (**Fig. 8**C).

Recording an action potential from subsequent electrodes along a microchannel enabled us to determine the propagation velocity and direction. The propagation velocities varied between 0.1 to 2.5 m/s, which is in same range as previously reported by Pan *et al.* (0.18 to 1.14 m s^{-1} in unmyelinated axons) [15]. In this study, we also evaluated changes in the propagation velocities in different segments of the same channel as well as in the same segment or channel over time. Changes in action potential velocity along the axon could be related to changes in thickness and curvature along the axon. We also observed an increased propagation velocity in all channels between 30 and 53 DIVs, which could possibly be related to increased axonal diameters or the fasciculation of axons. Such spatial and temporal changes in stimulus-driven action potential propagation velocity have been reported recently by Bakkum *et al.*, however in random cultures on dense microelectrode arrays [2]. In the present study, we evaluated the propagation velocity of signals derived from spontaneous network activity over time.

Bursts are spike flares within a short time window. Bursts are usually recorded simultaneously from different MEA electrodes, which shows that burst activity involves and propagates within large parts of the network [13]. We also evaluated how bursts propagate inside the microchannels. While individual monophasic spikes are able to propagate over long distances within a channel, bursts failed in reaching the microchannel endings in most cases (**Fig. 8**A). A significant difference in burst frequency on electrodes in proximal and distal parts of the microchannels confirmed the observed burst propagation fading along the microchannel (**Fig. 8**B). Because bursts are composed of individual spikes with different shapes, each of them will have its specific half-life for traveling along the channel. Fading spikes inside a burst will cause the burst to disintegrate along the channel. In consequence, a spike sequence that was categorized as a burst at the proximal end of a channel may not be recognized as a burst anymore at the distal end of a channel. Another mechanism for burst fading could be based on a phase cancelation effect. Signals with different shapes and phases can cancel each other out while traveling along the channel [21].

4.2 PDMS microchannels for the production of tissue-conformal *in vivo* MEAs for neuroprosthetic applications

Compared to stiff implants, flexible probes will more easily relieve the strain caused by micromotion forces that result from the relative displacement between the implant and the brain tissue. This may minimize chronic tissue damage or inflammation due to a better match in the stiffness of the probe and the brain microenvironment [19]. In this context, PDMS has potential as a scaffold material for neural interfaces [12, 14].

As thin sheets it can follow the curvature of a tissue and provide a uniform and tight contact [9]. Here, we exemplarily depicted the design and fabrication of a flexible *polyMEA* with 18 recording sites that can be implanted into the brain tissue. Impedance characteristics indicated that the electrodes performed well even in the low frequency range. At 1 kHz, their average impedance stayed at several hundred k Ω with an almost resistive behavior.

5 Acknowledgements

Many thanks to Marina Nanni, Francesca Succol and Claudia Chiabrera for their excellent assistance in cell culture preparation. Thanks to Francesco Difato and Mattia Pesce for their advice on imaging techniques. Intramural funding is highly appreciated.

6 References

1. Anderson JR, Chiu DT, Jackman RJ et al. (2000) Fabrication of Topologically Complex Three-Dimensional Microfluidic Systems in PDMS by Rapid Prototyping. Analytical Chemistry 72:3158-3164
2. Bakkum DJ, Frey U, Radivojevic M et al. (2013) Tracking axonal action potential propagation on a high-density microelectrode array across hundreds of sites. Nature communications 4:2181
3. Banker G, Goslin K (1998) Culturing Nerve Cells. The MIT Press, Cambridge
4. Bettinger CJ, Borenstein JT (2010) Biomaterials-based microfluidics for engineered tissue constructs. Soft Matter 6:4999-5015
5. Blau A, Murr A, Wolff S et al. (2011) Flexible, all-polymer microelectrode arrays for the capture of cardiac and neuronal signals. Biomaterials 32:1778-1786
6. Blau A, Neumann T, Ziegler C et al. (2009) Replica-moulded polydimethylsiloxane culture vessel lids attenuate osmotic drift in long-term cell cultures. Journal of biosciences 34:59-69
7. Claverol-Tinture E, Ghirardi M, Fiumara F et al. (2005) Multielectrode arrays with elastomeric microstructured overlays for extracellular recordings from patterned neurons. Journal of neural engineering 2:L1-7
8. Dworak BJ, Wheeler BC (2009) Novel MEA platform with PDMS microtunnels enables the detection of action potential propagation from isolated axons in culture. Lab on a Chip 9:404-410
9. Guo L, Meacham KW, Hochman S et al. (2010) A PDMS-based conical-well microelectrode array for surface stimulation and recording of neural tissues. IEEE Transactions on Bio-medical Engineering 57:2485-2494
10. Kim HJ, Park JW, Byun JH et al. (2012) Quantitative Analysis of Axonal Transport by Using Compartmentalized and Surface Micropatterned Culture of Neurons. Acs Chem Neurosci 3:433-438

11. Kim YT, Karthikeyan K, Chirvi S et al. (2009) Neuro-optical microfluidic platform to study injury and regeneration of single axons. Lab Chip 9:2576-2581
12. Lacour S, Benmerah S, Tarte E et al. (2010) Flexible and stretchable micro-electrodes for in vitro and in vivo neural interfaces. Medical and Biological Engineering and Computing 48:945-954
13. Maeda E, Robinson HP, Kawana A (1995) The mechanisms of generation and propagation of synchronized bursting in developing networks of cortical neurons. The Journal of neuroscience : the official journal of the Society for Neuroscience 15:6834-6845
14. Maghribi M, Hamilton J, Polla D et al. (2002) Stretchable Micro- Electrode Array. In: Microtechnologies in Medicine & Biology 2nd Annual International IEEE-EMB Special Topic Conference, p 80-83
15. Pan LB, Alagapan S, Franca E et al. (2011) Propagation of action potential activity in a predefined microtunnel neural network. Journal of neural engineering 8
16. Park J, Koito H, Li J et al. (2009) Microfluidic compartmentalized co-culture platform for CNS axon myelination research. Biomedical microdevices 11:1145-1153
17. Qin D, Xia Y, Whitesides GM (2010) Soft lithography for micro- and nanoscale patterning. Nature protocols 5:491-502
18. Ravula SK, Mcclain MA, Wang MS et al. (2006) A multielectrode microcompartment culture platform for studying signal transduction in the nervous system. Lab Chip 6:1530-1536
19. Subbaroyan J, Kipke DR (2006) The role of flexible polymer interconnects in chronic tissue response induced by intracortical microelectrodes--a modeling and an in vivo study. Conference proceedings : ... Annual International Conference of the IEEE Engineering in Medicine and Biology Society. IEEE Engineering in Medicine and Biology Society. Conference 1:3588-3591
20. Taylor AM, Blurton-Jones M, Rhee SW et al. (2005) A microfluidic culture platform for CNS axonal injury, regeneration and transport. Nature methods 2:599-605
21. Wang L, Riss M, Buitrago JO et al. (2012) Biophysics of microchannel-enabled neuron-electrode interfaces. Journal of neural engineering 9:026010
22. Wheeler BC, Brewer GJ (2010) Designing Neural Networks in Culture. Proceedings of the IEEE 98:398-406
23. Yang IH, Gary D, Malone M et al. (2012) Axon myelination and electrical stimulation in a microfluidic, compartmentalized cell culture platform. Neuromolecular medicine 14:112-118
24. Yun K-S, Yoon E (2008) Fabrication of complex multilevel microchannels in PDMS by using three-dimensional photoresist masters. Lab on a Chip 8:245-250

Figures

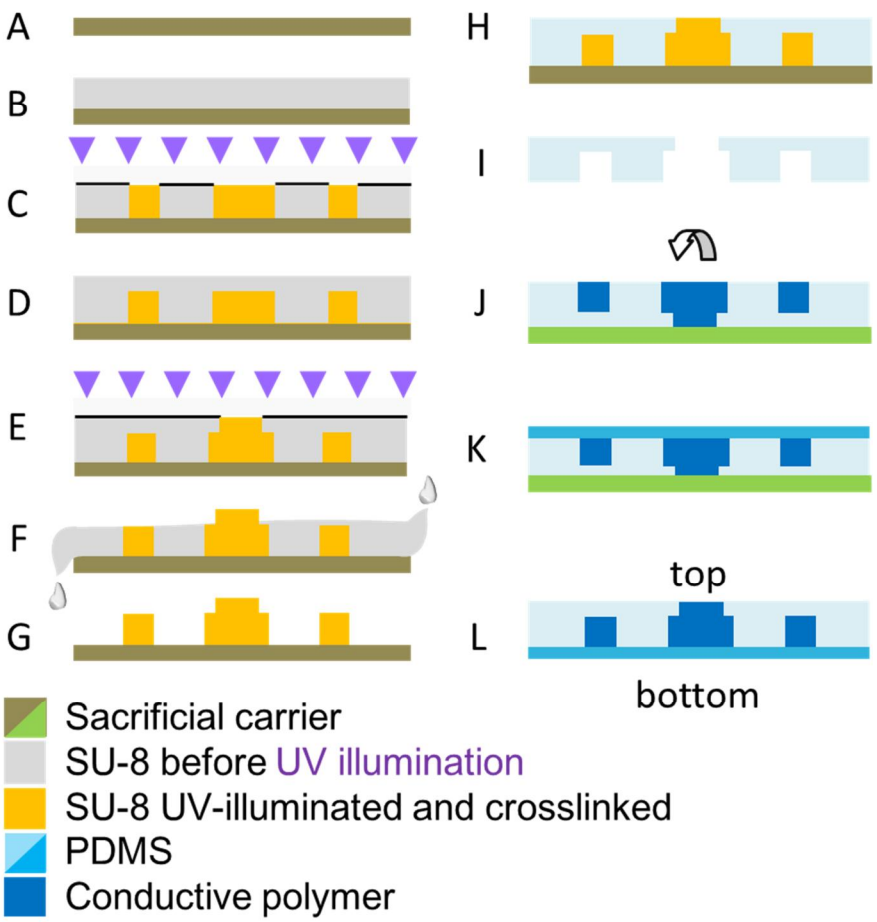

Fig. 1. Process flow of master generation (A-F) and microchannel replica molding from master in PDMS (G-I). The scaffold can either be used directly in neural guidance studies or be functionalized *e.g.*, with conductive polymers (J-L).

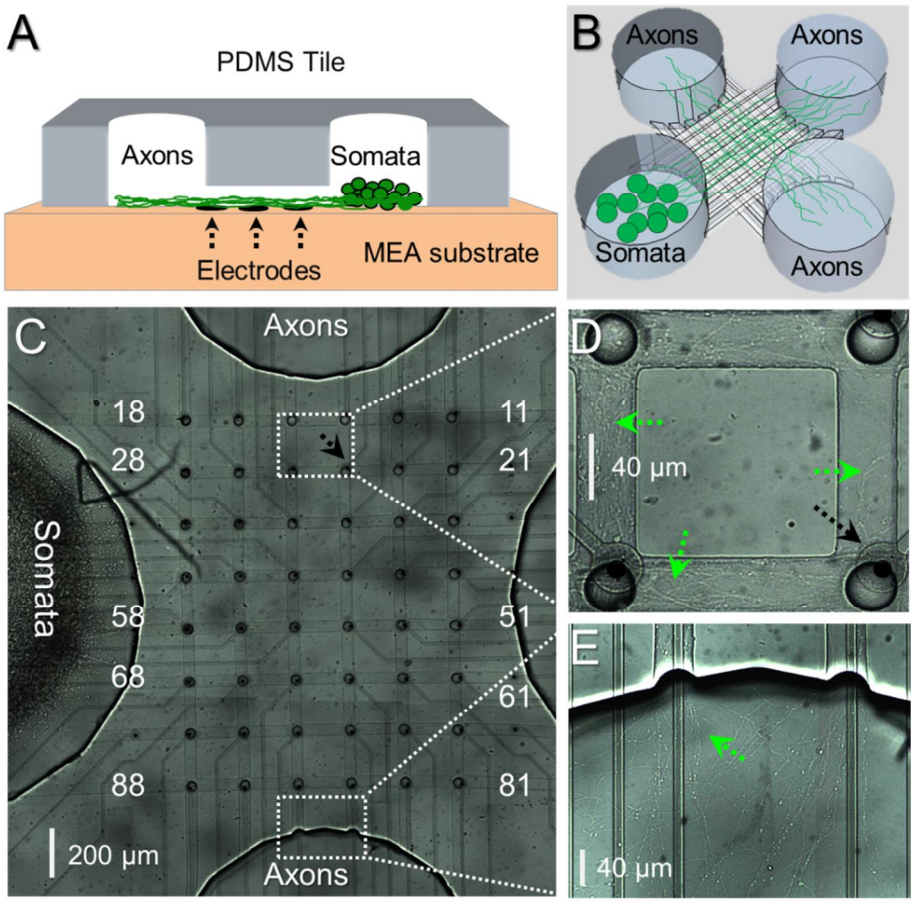

Fig. 2. PDMS microchannel tiles on MEAs for neural network compartmentalization A) A schematic cross-section of a microchannel and the reservoirs shows how microchannels selectively let axons grow on top of an electrode row while preventing cell bodies to enter. B) PDMS microstructure including four big reservoirs interconnected by an 8 × 8 matrix of channels. C) Cells seeded in a somal compartment (left) had grown their axons after 9 DIV through the entire length of a microchannel into the empty axonal compartment. D) Magnified view of the axons inside the channels between electrodes 15-14 and 25-24. E) Magnified view of axons entering the axonal compartment. Black arrows indicate at an electrode and green arrows point at axons.

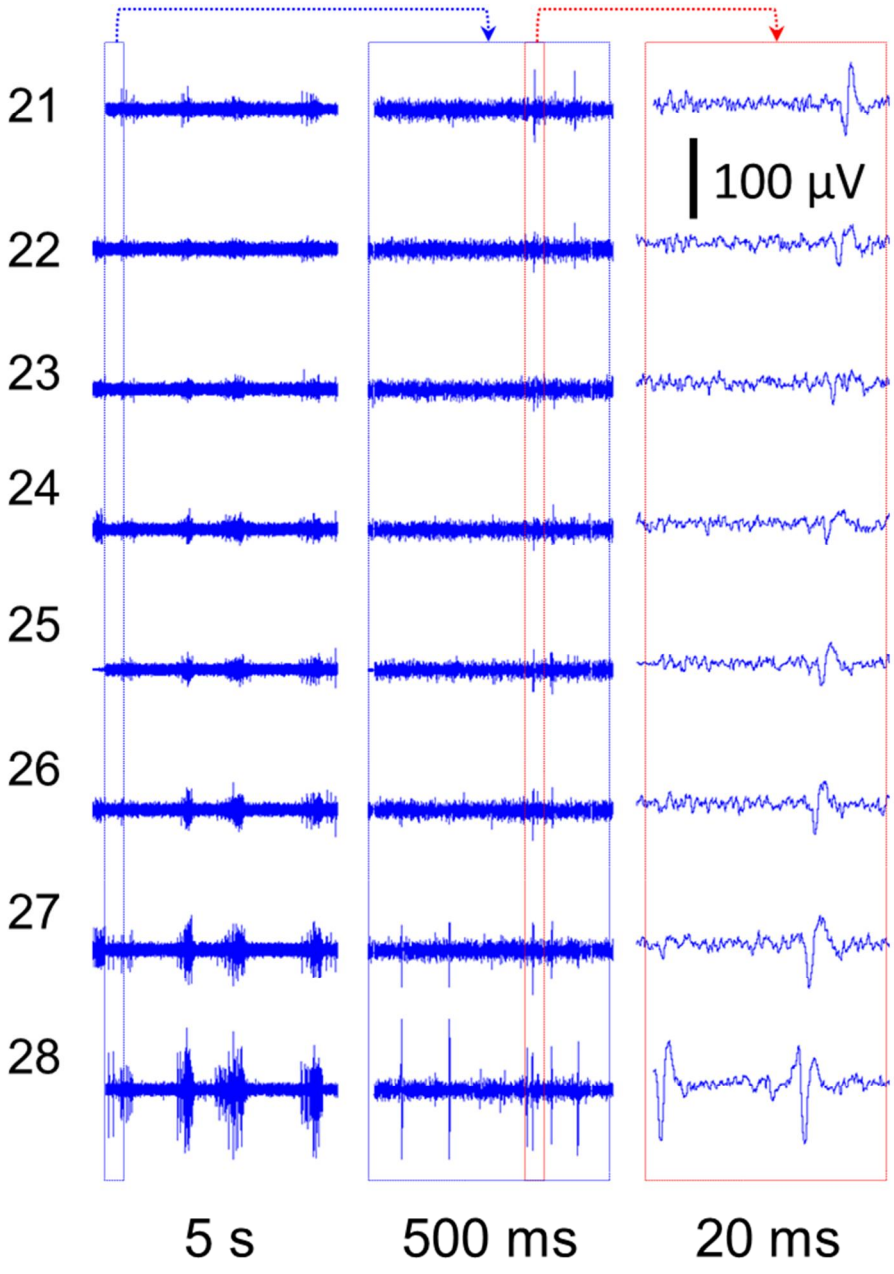

Fig. 3. Sample recording from electrodes in channel 2 at 30 DIV. The right panel shows the magnified propagating signal along the full length of the channel from electrode 28 toward electrode 21 (see **Fig. 2**C).

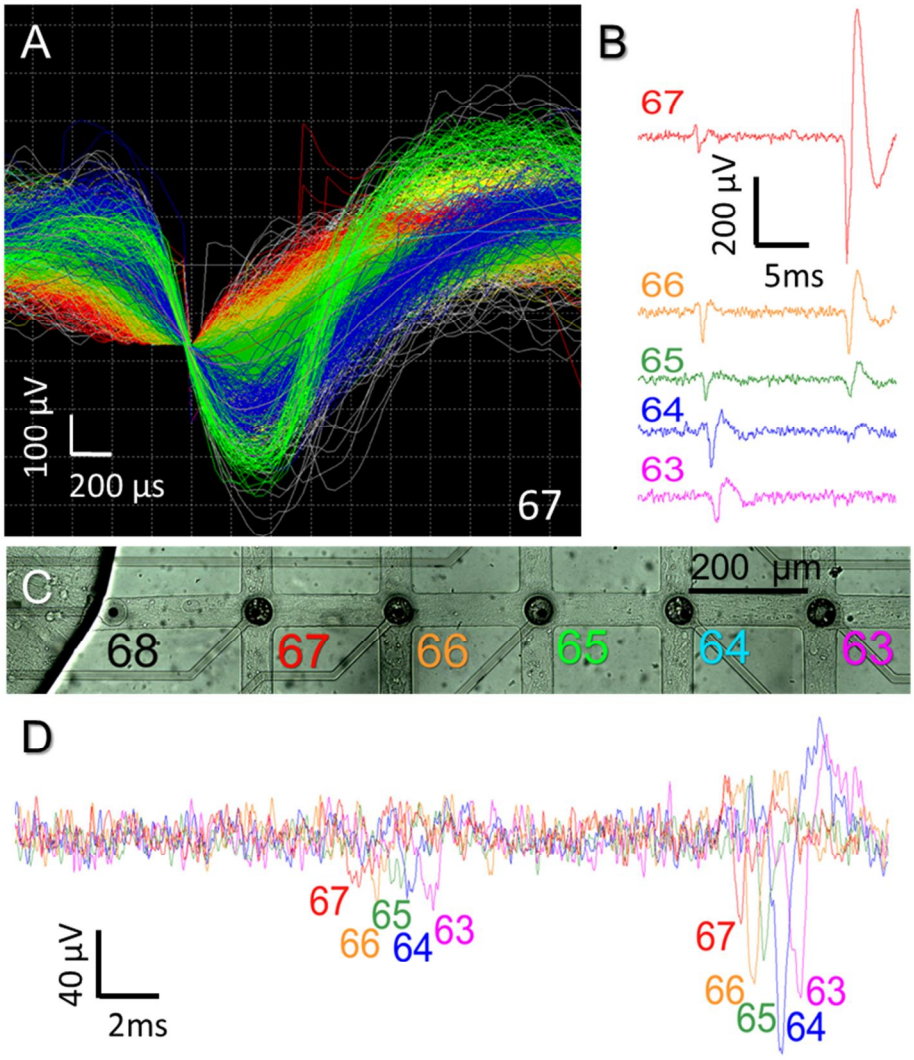

Fig. 4. Signals with different amplitudes and shapes were propagating in channels. A) Signal sorting for electrode 67 shows five different waveforms that were recorded by this electrode. B) Shape and propagation length of monophasic and biphasic signals in channel 6 from electrode 67 to 63 (C). D) Overlaid signals recorded from electrodes 67 to 63 show the propagation delays for a signal traveling within an axon over sequential electrodes.

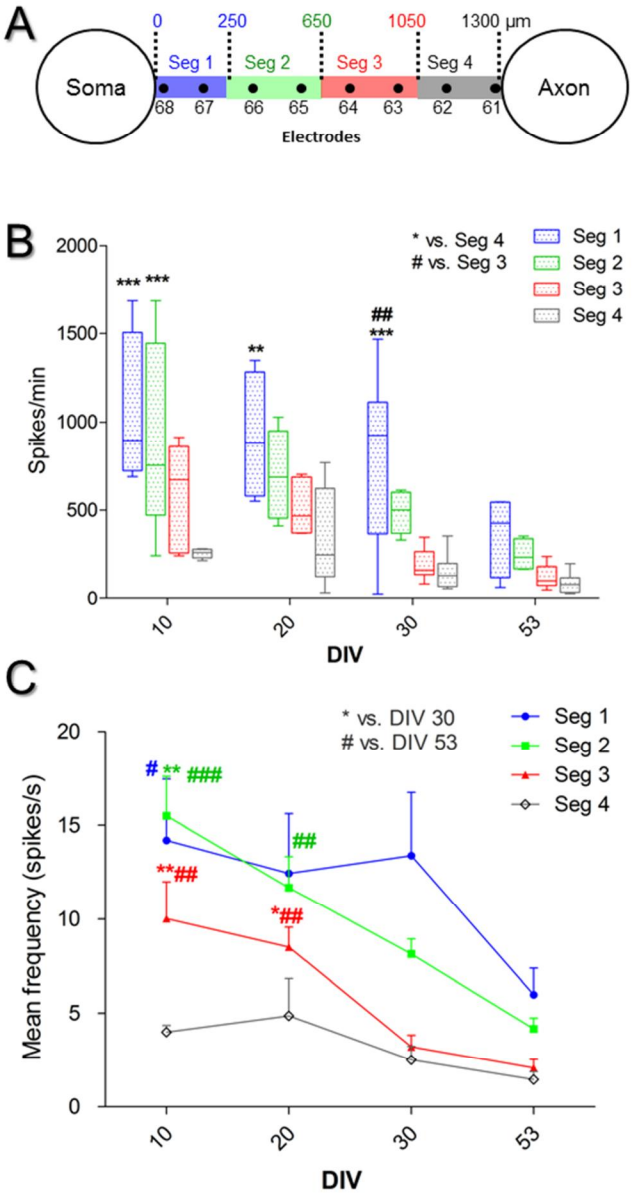

Fig. **5.** The spike frequency decreased along a channel and over time. A) Each microchannel was divided into four sections for a spike frequency analysis in the following way: segment 1 (Seg 1 = 250 µm from channel entrance), Seg 2 (250-650 µm), Seg 3 (650-1050 µm), Seg 4 (1050-1300 µm). Each segment represents data that was collected from two adjacent electrodes. B) Spike frequency along the channel. Each bar represents the spike frequency range in one

segment (color) on the mentioned day. The mean spike frequency was calculated by averaging the number of spikes per minute in a selected segment of channels 2, 5 and 6. A two-way ANOVA was applied for comparing the mean values between different segments on the mentioned day. * vs. Seg 4 and # vs. Seg 3 at the same DIV. C) Spike frequency evolution over time. Each line represents the changes in the mean spike frequency of the same segment (averaged over three channels) at different days. A one-way repeated measures ANOVA was applied for analyzing the mean frequency between different DIVs in each segment. * vs. DIV 30 and # vs. DIV 53 of the same segment . * or # $p < 0.05$, ** or ## $p < 0.01$ and *** or ### $p < 0.001$.

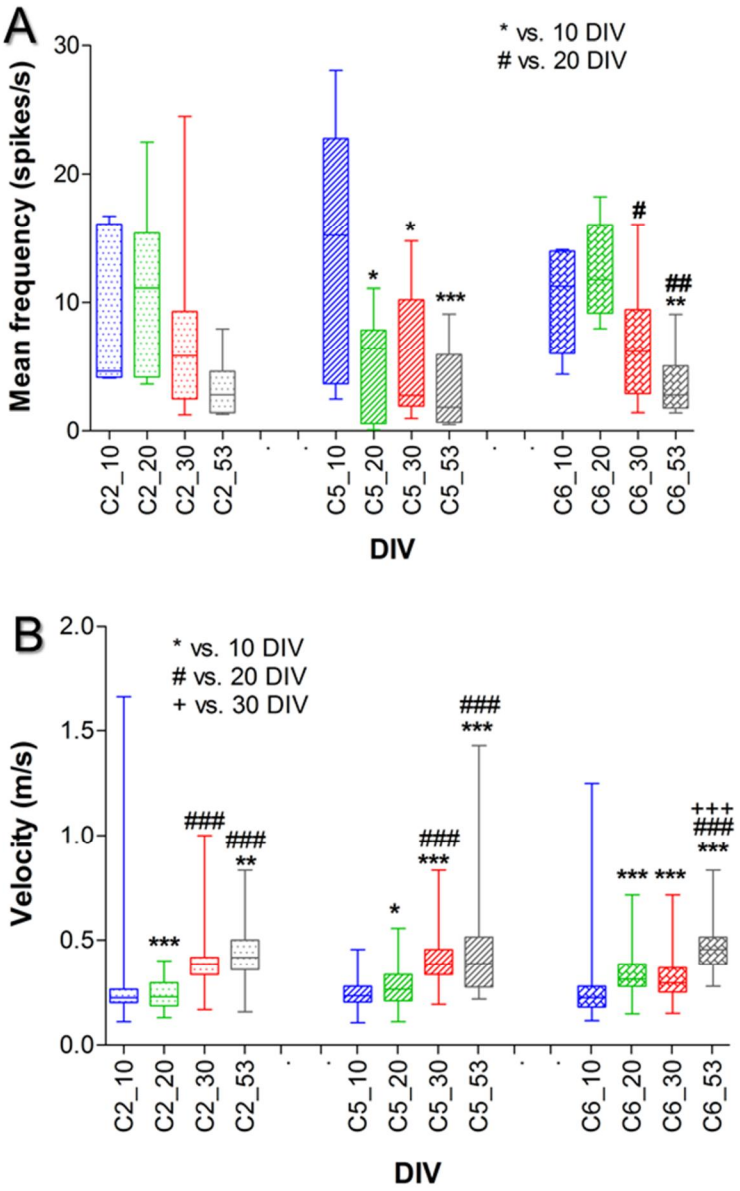

Fig. 6. Different profiles for spike frequency and propagation velocity in three evaluated channels over time. A) Each bar represents the range of spike frequencies in one channel on the mentioned day. X-axis denominators code for the channel number followed by the DIV on which the recording was performed. One-way repeated measures ANOVA applied for analyzing the mean frequency between different DIVs in each channel. * vs. DIV 10 and # vs. DIV 20 in same channel. B) Mean propagation speed in each channel for a given DIV. After calculating the velocity between each electrode pair in a channel, the mean propagation speed was deter-

mined by averaging the velocities of all pairs. Each bar represents the range of propagation speed in one channel at the mentioned day. One-way repeated measures ANOVA applied for analyzing the mean velocity between different DIVs in each channel. * vs. DIV 10, # vs. DIV 20 and + vs. DIV 30 in same channel. * or # $p < 0.05$, ** or ## $p < 0.01$ and ***, ### and +++ $p < 0.001$. Electrodes 27, 52 and 62 did not record any spikes at 10 and 20 DIV. Therefore, the velocity was estimated by dividing the time delay between two nearby electrodes by a distance of 400 µm.

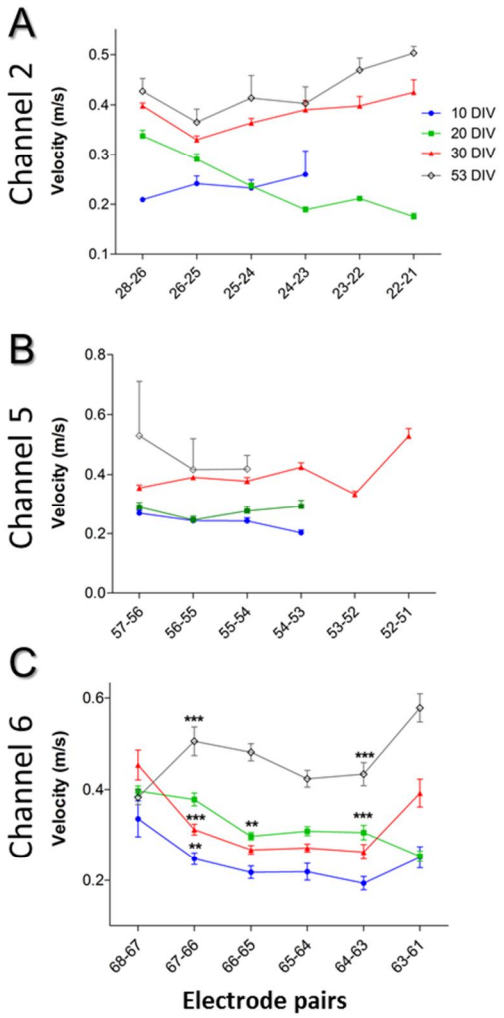

Fig. 7. Changes in the signal propagation velocity along the axon in different channels. The propagation velocity was calculated by dividing the constant distance between each electrode pair by the temporal delay between time stamps. A and B) in channels 2 and 5: no significant differences in the propagation velocity between two subsequent electrode pairs could be detected. C) In channel 6, however, the velocity decreased or increased significantly along the axon at different days. One-way repeated measures ANOVA was applied for analyzing the mean propagation velocity between two subsequent electrode pairs at the mentioned day. *$p < 0.05$, **$p < 0.01$ and ***$p < 0.001$ vs. mean propagation speed between previous electrode pairs. For all channels, the propagation speed was calculated for 30 randomly selected propagating signals at different time points during the recording window (1 min).

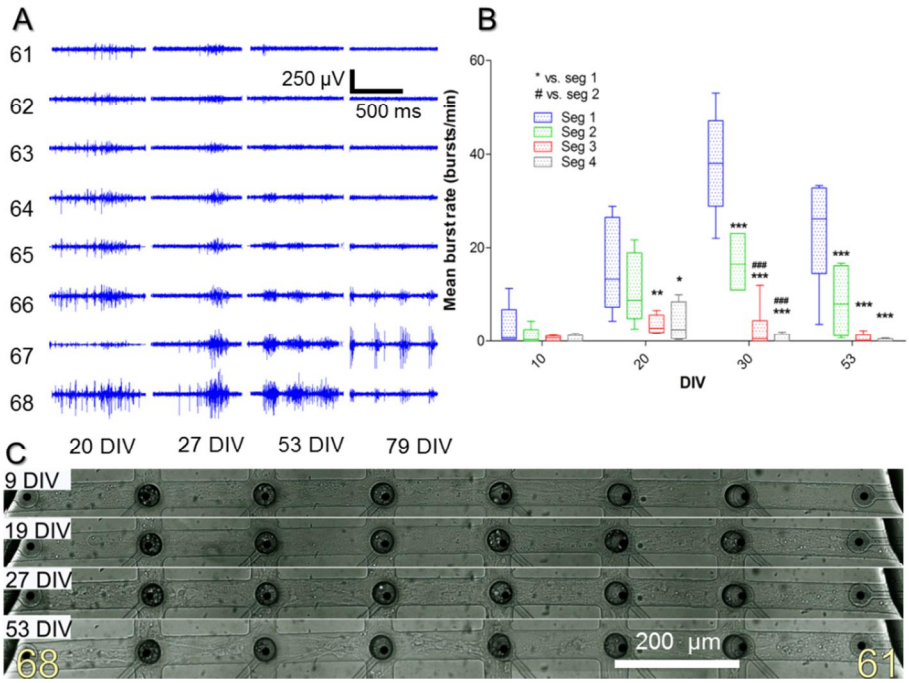

Fig. 8. Burst propagation along channels. A) Raw signals from channel 6 (electrodes 68-61) at different DIVs. B) Mean burst frequency in different segments of three channels. After burst detection, the burst frequency was calculated for each channel segment of channels 2, 5 and 6, and then averaged for all three channels. Each bar represents the burst frequency range in one segment of all three channels. Two-way ANOVA applied for analyzing the mean burst rate between two segments of the same channel at the mentioned day. * vs. seg 1 and # vs. seg 2. * $p < 0.05$, ** $p < 0.01$ and *** or ### $p < 0.001$. C) Changes in morphology along channel 6 (electrodes 68 to 61) over 53 DIV.

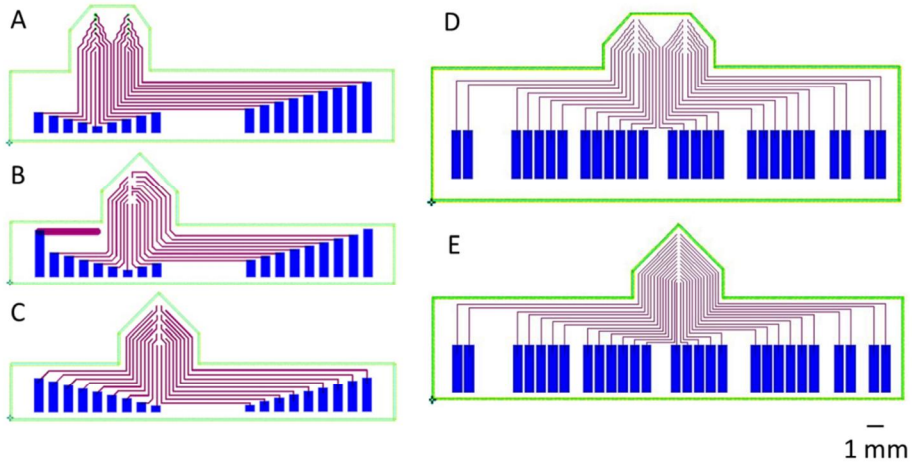

Fig. 9. Five *polyMEA* design examples for recording from various brain areas. The number of electrodes is the same in A, B and C (18) and in D and E (28). Design B with two separate electrode fields is suitable for the local recording at two specific depths while designs A, C, D, and E are universal probes with equal electrode pitches along their insertion shafts. The sharpened probe tips in designs B, C and E may facilitate probe insertion into the brain. Electrode pitch and diameter, wire widths and pitches are different in these designs.

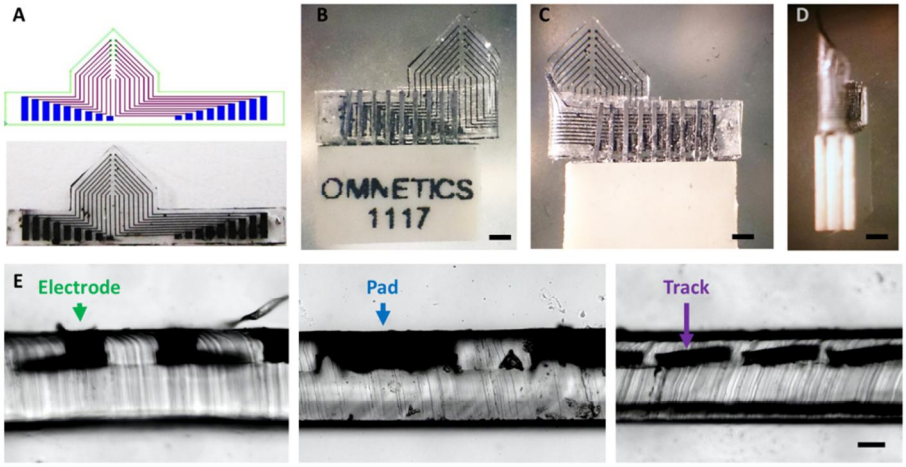

Fig. 10. Overall device layout and connecting scheme for an *in vivo polyMEA* with 2 x 9 electrode array. A) CAD design and resulting device with tracks and electrodes made from a conductive polymer composite; pad width: 414 µm. B-D) *polyMEA* squeeze-clamped between an Omnetics (A79006-001) 0.757 mm pitch, double-row pin connector (front, back and side). In this case, no extra PDMS sealing coat was applied to the connector and the *polyMEA* yet. E) Cross section views of the *polyMEA* electrodes (left), pads (middle) and buried tracks (right). Scale bars: 1 mm (B-D), 100 µm (E).

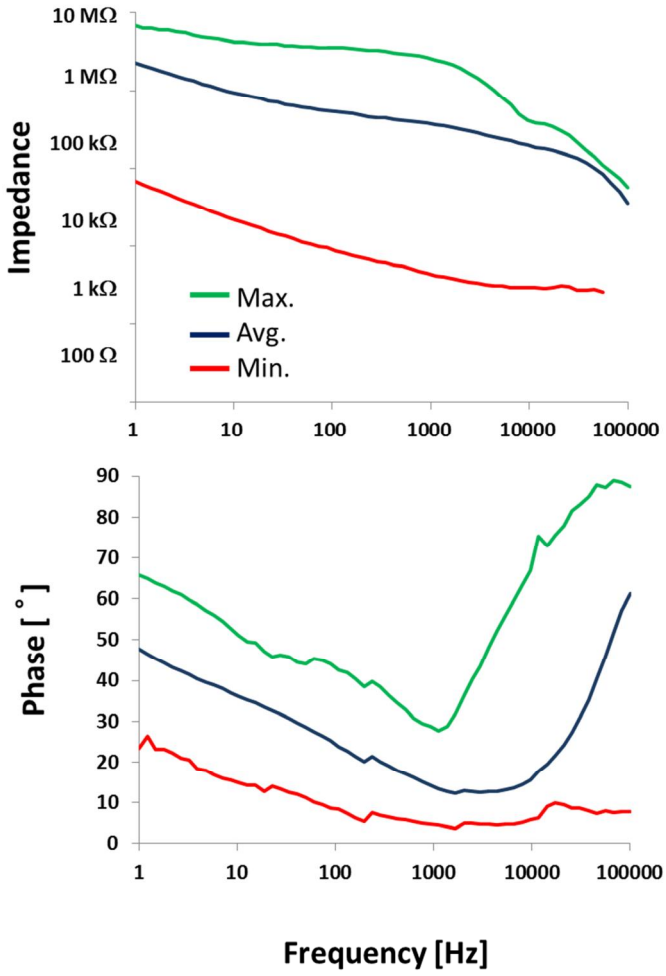

Fig. 11. Impedance characteristics of a *polyMEA* with a 2 x 9 electrode array. Electrode diameters ranged from 50 µm to 130 µm by 10 µm increments. Comparison of the average (Avg.) and extreme (Min., Max.) electrode impedances in a Bode magnitude plot (left) and of their capacitive-resistive characteristics in a phase plot (right).

Table

Table 1. Feature sizes of a universal *in vivo polyMEA* with 2 x 9 electrode array.

Parameter	Size [µm]
Maximum electrode site diameter	130
Minimum electrode site diameter	50
Vertical electrode center-to-center pitch	300
Horizontal electrode center-to-center pitch	300
Vertical electrode array dimension (center-to-center)	2400
Shaft width	5,370
Shaft thickness	280.6
Shaft length	3,920
Track width	50